

To appear in the *International Journal of Computational Fluid Dynamics*  
 Vol. 00, No. 00, 00 Month 20XX, 1–14

## Symmetry breaking and preliminary results about a Hopf bifurcation for incompressible viscous flow in an expansion channel

A. Quaini<sup>a\*</sup>, R. Glowinski<sup>a</sup> and S. Čanić<sup>a</sup>

<sup>a</sup>*Department of Mathematics, University of Houston, Houston, TX 77204, USA*

(...)

This computational study shows, for the first time, a clear transition to 2D Hopf bifurcation for laminar incompressible flows in symmetric plane expansion channels. Due to the well-known extreme sensitivity of this study on computational mesh, the critical Reynolds numbers for both the known symmetry-breaking (pitchfork) bifurcation and Hopf bifurcation were investigated for several layers of mesh refinement. It is found that under-refined meshes lead to an overestimation of the critical Reynolds number for the symmetry-breaking and an underestimation of the critical Reynolds number for the Hopf bifurcation.

**Keywords:** expansion flow; symmetry breaking; Hopf-bifurcation; computational fluid dynamics; stability of incompressible viscous flows.

### 1. Introduction

The dynamics of an incompressible, Newtonian, and viscous fluid in a planar contraction-expansion channel has long been of interest from both theoretical and practical perspectives (see, e.g., Moffatt (1964); Durst et al. (1974); Cherdron et al. (1978); Drikakis (1997); Sobey and Drazin (1986); Fearn et al. (1990); Hawa and Rusak (2001); Mishra and Jayaraman (2002)). The simplicity of the geometry, which may be partially characterized by the expansion ratio  $\lambda = W/w$  (see Fig. 1(a)), and the fact that it yields a complex flow have made it a popular choice for use in testing computational models. See, e.g., Fearn et al. (1990); Drikakis (1997); Hawa and Rusak (2001); Mishra and Jayaraman (2002) and references therein. Practical applications include equipments such as heat exchangers, combustion chambers, and mixing vessel. An application that motivated the present study is the flow of blood through a regurgitant mitral valve, where it has been observed that depending on the Reynolds number and the regurgitant mitral valve orifice shape, the regurgitant jet bifurcates from the symmetric one to an asymmetric one, known in cardiology as Coanda effect Gingham (2007); Wang et al. (2015); Quaini et al. (2010).

In the two-dimensional geometry reported in Fig.1(a), as the Reynolds number  $Re$  (see (3) for the definition) increases from zero, the sequence of events is as follows. For sufficiently small value of  $Re$  (e.g., 0.01) a steady symmetric flow is observed. Moffatt eddies form (see Moffatt (1964)) close to the corners both upstream of the contraction and downstream of the expansion. See Fig. 2(a). The uniqueness of this solution is proved in Serrin (1959). As the inertial effects of fluid become more important, the Moffatt eddies upstream of the contraction gradually diminish in size and two recirculation regions of equal size develop downstream of the expansion (see, e.g., the experimental studies in Durst et al. (1974); Cherdron et al. (1978)). See Fig. 2(b). As the Reynolds number increases, flow symmetry about the central line is initially maintained and the downstream recirculation length increases progressively (see Durst et al. (1974); Cherdron et al.

---

\*Corresponding author. Email: quaini@math.uh.edu

(1978)). Above a certain critical Reynolds number denoted by  $Re_{sb}$ , a steady asymmetric solution is observed: the downstream recirculation zone expands while the other shrinks (see Drikakis (1997); Revuelta (2005)). See Fig. 2(c). This asymmetric solution remains stable for a certain range of  $Re$  and asymmetries become stronger with the increasing Reynolds number, as shown in Mishra and Jayaraman (2002). The formation of stable asymmetric vortices in 2D planar expansion is attributed to the Coanda effect (see Wille and Fernholz (1965)): an increase in velocity near one wall will lead to a decrease in pressure near that wall and once a pressure difference is established across the channel it will maintain the asymmetry of the flow. The value of  $Re_{sb}$  has been identified for different expansion ratios  $\lambda$ . In particular, it was found that  $Re_{sb}$  decreases with increasing value of  $\lambda$  (see Drikakis (1997); Revuelta (2005)).

The numerical computations of Sobey and Drazin (1986), and Fearn et al. (1990), together with the linear stability analysis of Shapira et al. (1990) indicate that the symmetry breaking occurs as a result of a supercritical pitchfork bifurcation in the solution of the Navier-Stokes equations, i.e., above  $Re_{sb}$  two stable solutions co-exist (see Battaglia et al. (1997)). In Sobey and Drazin (1986) it was shown that an unstable solution also exists. Bifurcation theory allows to clarify the nature of the multiplicity of possible flows, whereas a (numerical or laboratory) experiment will give one or the other of the stable symmetric solutions. In Fearn et al. (1990), the origin of steady asymmetric flows in a symmetric sudden expansion is studied using both experimental and numerical techniques and they calculated stable and unstable branches. Reference Hawa and Rusak (2001) explains the loss of symmetric stability as a result of the interaction between the effects of viscous dissipation, the downstream convection of perturbations by the base symmetric flow, and the upstream convection induced by 2D asymmetric disturbances.

At larger Reynolds numbers the flow becomes increasingly complex and other bifurcations occur. See Fig. 2(d). In Sobey and Drazin (1986) it was found that as  $Re$  is increased there is a turning point (a transition from a stable to an unstable steady flow, when a simple real eigenvalue of a mode increases through zero as  $Re$  reaches a certain value) and then four stable asymmetric steady solutions appear. At a further increase of  $Re$ , the flow becomes unsteady and the existence of a Hopf bifurcation is deduced (see Sobey and Drazin (1986)), although, to the best of our knowledge, the bifurcation point has never been calculated for a given value of  $\lambda$ . In Fearn et al. (1990), the authors tried but failed to find experimental evidence of a 2D Hopf bifurcation. They suggest that the three-dimensional effects in their experimental set-up prevented the onset of the Hopf bifurcation. On the other hand, the work in Lanzerstorfer and Kuhlmann (2012) detected oscillatory instability in 2D channels but only by certain *three-dimensional perturbations*.

In this work, we show by means of computational experiments that a Hopf bifurcation does occur in the 2D expansion channel without considering 3D perturbations, and we identify the corresponding critical value of the Reynolds number for a given expansion ratio  $\lambda$ : at a certain critical Reynolds number, that we denote by  $Re_H$ , the asymmetric solution loses its stability and a one-parameter family of periodic solutions bifurcates from the steady solution. A Hopf bifurcation is encountered when a pair of complex conjugate eigenvalues of the linearization around the steady solution crosses the imaginary axis of the complex plane as  $Re$  increases.

In order to identify the value of  $Re_H$  for a given expansion ratio, the linear hydrodynamic stability of a steady solution needs to be studied. When the fluid domain is characterized by two or three dimensions with nonperiodic boundary conditions (as in our case), the formulation of the stability problem requires solving a partial differential eigenvalue problem. In the particular case of 2D incompressible flows, the analysis of the linear stability involves the solution of a biharmonic eigenvalue problem in 2D (see, e.g., Bayly et al. (1988)). We refer the reader to Dijkstra et al. (2014) for a review on numerical methods for stability analysis based on linearized eigenvalue problems. Another possibility is to write the eigenvalue problem for the coupled system of equations for velocity and pressure, as in Fortin et al. (1997). An alternative to the eigenvalue problem approach is the direct simulation of the flow to characterize the asymptotic behavior (steady, periodic, quasiperiodic or chaotic) of the solution depending on the value of the relevant parameter, i.e. the Reynolds number. The direct simulation can be rather expensive in terms of computational time,

since long simulations are often required, but it has the advantage of making the flow beyond the first Hopf bifurcation accessible. In this paper we use the latter approach.

The objectives of this work are: (i) to validate the critical Reynolds number of the symmetry breaking bifurcation  $Re_{sb}$  in a plane contraction-expansion channel against the results in Oliveira et al. (2008) (expansion ratio  $\lambda = 15.4$ ) and Drikakis (1997) ( $\lambda = 6$ ), (ii) to investigate, through direct simulation, the critical Reynolds number of the Hopf bifurcation  $Re_H$  in the channel with  $\lambda = 6$ , and (iii) to check the effect of mesh refinement on the value of both  $Re_{sb}$  and  $Re_H$ .

The outline of the paper is as follows. In Section 2 we state the problem, discuss the numerical methods used for the time and space discretization and describe the solution of the associated linear system. In Section 3, we report on the results of the validation against Oliveira et al. (2008) and Drikakis (1997). In Section 4, we discuss the identification of  $Re_H$  for expansion ratio  $\lambda = 6$ . Finally, conclusions are in Section 5.

## 2. Numerical modeling

The motion of an incompressible viscous fluid in a spatial domain of dimension  $d$  (denoted hereafter by  $\Omega$ ) over a time interval of interest  $(0, T)$  is described by the incompressible Navier-Stokes equations

$$\rho \left( \frac{\partial \mathbf{u}}{\partial t} + \mathbf{u} \cdot \nabla \mathbf{u} \right) - \nabla \cdot \boldsymbol{\sigma} = \mathbf{0} \quad \text{in } \Omega \times (0, T), \quad (1)$$

$$\nabla \cdot \mathbf{u} = 0 \quad \text{in } \Omega \times (0, T), \quad (2)$$

where  $\rho$  is the fluid density,  $\mathbf{u}$  is the fluid velocity, and  $\boldsymbol{\sigma}$  the Cauchy stress tensor. For Newtonian fluids,  $\boldsymbol{\sigma}$  has the following expression

$$\boldsymbol{\sigma}(\mathbf{u}, p) = -p\mathbf{I} + 2\mu\boldsymbol{\epsilon}(\mathbf{u}),$$

where  $p$  is the pressure,  $\mu$  is the fluid dynamic viscosity, and

$$\boldsymbol{\epsilon}(\mathbf{u}) = \frac{1}{2}(\nabla \mathbf{u} + (\nabla \mathbf{u})^T)$$

is the strain rate tensor. In eq. (1)-(2), it is supposed that no body force is applied to the system.

Equations (1)-(2) need to be supplemented with initial and boundary conditions, which will be specified in Sec. 3 for the each problem under consideration.

The Reynolds number  $Re$  can be used to characterize the flow regime. It is defined as:

$$Re = \frac{\rho LU}{\mu}, \quad (3)$$

where  $L$  is a characteristic length and  $U$  is a characteristic velocity. The Reynolds number can be thought of as the ratio of inertial forces to viscous forces. For large Reynolds numbers inertial forces are dominant over viscous forces and vice versa.

The flow in the 2D geometry reported in Fig. 1(a) can be seen as the limiting case of a 3D flow in the domain shown in Fig. 1(b) for channel depth  $H$  tending to infinity. For the 3D problem, the characteristic length  $L$  is given by the hydraulic diameter of the contraction channel, i.e.  $L = 2Hw/(H + w)$ , thus (3) becomes:

$$Re_{3D} = \frac{\rho U}{\mu} \frac{2Hw}{H + w}. \quad (4)$$

By letting  $H \rightarrow \infty$  in eq. (4), we define the Reynolds number for the 2D problem

$$Re = 2 \frac{\rho U w}{\mu}. \quad (5)$$

We define  $Re$  as in (5) with the purpose of comparing our results with Oliveira et al. (2008) (see Sec. 3). As characteristic velocity  $U$  in (5), we take the average velocity in the contraction channel. So, if we denote by  $U_{\max}$  the maximum velocity in the contraction channel and assume that the contraction channel is long enough to have a fully developed parabolic velocity profile, we have  $U = 2U_{\max}/3$ .

For the variational formulation of the fluid problem (1)-(2), we indicate with  $L^2(\Omega)$  the space of square integrable functions in a spatial domain  $\Omega$  and with  $H^1(\Omega)$  the space of functions in  $L^2(\Omega)$  with first derivatives in  $L^2(\Omega)$ . We use  $(\cdot, \cdot)_{\Omega}$  and  $\langle \cdot, \cdot \rangle_{\Omega}$  to denote the  $L^2$  product and a duality pair in  $\Omega$ , respectively. Moreover, let us define:

$$[H_0^1(\Omega)]^d = \left\{ \mathbf{v} \in [H^1(\Omega)]^d, \mathbf{v}|_{\Gamma_D} = \mathbf{0} \right\},$$

where  $\Gamma_D$  is the part of the domain boundary on which a Dirichlet condition is imposed.

The variational formulation of the fluid problem (1)-(2) is: given  $t \in (0, T)$ , find  $(\mathbf{u}, p) \in [H^1(\Omega)]^d \times L^2(\Omega)$  such that

$$\rho \left( \frac{\partial \mathbf{u}}{\partial t}, \mathbf{v} \right)_{\Omega} + \mathcal{N}(\mathbf{u}; [\mathbf{u}, p], [\mathbf{v}, q])_{\Omega} = 0, \quad \forall (\mathbf{v}, q) \in [H_0^1(\Omega)]^d \times L^2(\Omega), \quad (6)$$

with

$$\begin{aligned} \mathcal{N}(\mathbf{u}; [\mathbf{u}, p], [\mathbf{v}, q])_{\Omega} = & 2\mu(\boldsymbol{\epsilon}(\mathbf{u}), \boldsymbol{\epsilon}(\mathbf{v}))_{\Omega} + \rho \int_{\Omega} (\mathbf{u} \cdot \nabla \mathbf{u}) \cdot \mathbf{v} d\Omega - (p, \nabla \cdot \mathbf{v})_{\Omega} \\ & + (\nabla \cdot \mathbf{u}, q)_{\Omega}. \end{aligned} \quad (7)$$

## 2.1. Discretization

For the time discretization of equations (1)-(2) we chose the Backward Differentiation Formula of order 2 (BDF2, see Quarteroni et al. (2007)). Given  $\Delta t \in \mathbb{R}$ , let us set  $t^n = t_0 + n\Delta t$ , with  $n = 0, \dots, N_T$  and  $T = t_0 + N_T\Delta t$ . Problem (1)-(2) discretized in time reads: given  $\mathbf{u}^n$ , for  $n \geq 1$ , find the solution  $(\mathbf{u}^{n+1}, p^{n+1})$  of the system:

$$\rho \frac{3\mathbf{u}^{n+1} - 4\mathbf{u}^n + \mathbf{u}^{n-1}}{2\Delta t} + \rho \mathbf{u}^{n+1} \cdot \nabla \mathbf{u}^{n+1} - \nabla \cdot \boldsymbol{\sigma}(\mathbf{u}^{n+1}, p^{n+1}) = \mathbf{0} \quad \text{in } \Omega, \quad (8)$$

$$\nabla \cdot \mathbf{u}^{n+1} = 0 \quad \text{in } \Omega. \quad (9)$$

For the space discretization, we introduce a conformal and quasi-uniform partition  $\mathcal{T}_h$  of  $\Omega$  made up of a certain number of triangles. Let  $V_h \subset [H^1(\Omega)]^d$ ,  $V_{0,h} \subset [H_0^1(\Omega)]^d$ ,  $Q_h \subset L^2(\Omega)$  be the finite element spaces approximating  $[H^1(\Omega_0^f)]^d$ ,  $[H_0^1(\Omega_0^f)]^d$ , and  $L^2(\Omega_0^f)$ , respectively. We introduce the Lagrange basis  $\{\phi_i\}_{i=1}^{\mathcal{N}_v}$  and  $\{\pi_i\}_{i=1}^{\mathcal{N}_p}$  associated to  $V_h$  and  $Q_h$  (respectively), where  $\mathcal{N}_v$  is the number of nodes for the velocity approximation and  $\mathcal{N}_p$  is number of nodes for the pressure approximation.

In order to write the matrix version of the fully discretized problem, we set:

- The mass matrix:  $M_{i,j} = \int_{\Omega} \phi_j \phi_i$ .
- The stiffness matrix:  $K_{i,j} = 2 \int_{\Omega} \boldsymbol{\epsilon}(\phi_j) : \boldsymbol{\epsilon}(\phi_i)$ .
- The matrix associated with the convective term:  $N_{i,j}(\mathbf{u}^{n+1}) = \int_{\Omega} (\mathbf{u}^{n+1} \cdot \nabla) \phi_j \cdot \phi_i$ .

- The matrix associated with operator  $(-\nabla \cdot)$ :  $B_{i,j} = -\int_{\Omega} (\nabla \cdot \phi_j) \pi_i$ .

The full discretization of problem (1)-(2) yields the following nonlinear system

$$\rho \frac{3}{2\Delta t} M \mathbf{U}^{n+1} + \mu K \mathbf{U}^{n+1} + \rho N(\mathbf{u}^{n+1}) \mathbf{U}^{n+1} + B^T \mathbf{P}^{n+1} = \mathbf{b}_u^{n+1}, \quad (10)$$

$$B \mathbf{U}^{n+1} = \mathbf{b}_p^{n+1}, \quad (11)$$

where  $\mathbf{U}^{n+1}$  and  $\mathbf{P}^{n+1}$  are the arrays of nodal values for velocity and pressure. The arrays  $\mathbf{b}_u^{n+1}$  and  $\mathbf{b}_p^{n+1}$  account for the contributions of the solution at the previous time steps and the contribution that the boundary nodes give to the internal nodes.

Set  $C = \rho \frac{3}{2\Delta t} M + \mu K + \rho N(\mathbf{u}^{n+1})$ . We can rewrite (10)-(11) in the form

$$A \mathbf{X}^{n+1} = \mathbf{b}^{n+1}, \quad (12)$$

where

$$A = \begin{bmatrix} C & B^T \\ B & 0 \end{bmatrix}, \quad \mathbf{X}^{n+1} = \begin{bmatrix} \mathbf{U}^{n+1} \\ \mathbf{P}^{n+1} \end{bmatrix}, \quad \mathbf{b}^{n+1} = \begin{bmatrix} \mathbf{b}_u^{n+1} \\ \mathbf{b}_p^{n+1} \end{bmatrix}.$$

In order to deal with the convective term nonlinearity, we use a fixed-point algorithm. At every fixed-point iteration, we use a multifrontal parallel sparse direct solver (see, e.g., Davis and Duff (1997)) to solve the linearized version of system (12).

The standard Galerkin approximation of the incompressible Navier-Stokes equations reported in (10)-(11) is unstable if the pair  $(Q_h, V_h)$  does not satisfy the well-known *inf-sup* condition (see, e.g. Quarteroni and Valli (1994)). In order to be able to use equal order velocity-pressure pairs (which are not inf-sup stable, like the  $\mathbb{P}_1 - \mathbb{P}_1$  finite elements used in Sec. 3 and 4), we resort to a stabilized formulation. The obvious advantage of this choice is that  $\mathcal{N}_v = \mathcal{N}_p$ .

The stabilization method that we adopt is the orthogonal subgrid scales (OSS) technique proposed in Codina (2002): it provides pressure stability and stabilizes the convective term for high Reynolds numbers. Let  $\mathbf{u}_h$  and  $p_h$  be the space discrete velocity and pressure. The stabilized version of the problem under consideration reads: given  $t \in (0, T)$ , find  $(\mathbf{u}_h, p_h) \in V_h \times Q_h$

$$\rho \left( \frac{\partial \mathbf{u}_h}{\partial t}, \mathbf{v}_h \right)_{\Omega} + \mathcal{N}_s(\mathbf{u}_h; [\mathbf{u}_h, p_h], [\mathbf{v}_h, q_h])_{\Omega} = 0, \quad \forall (\mathbf{v}_h, q_h) \in V_{0,h} \times Q_h,$$

where  $\mathcal{N}(\mathbf{u}_h; [\mathbf{u}_h, p], [\mathbf{v}_h, q_h])_{\Omega}$  in the discretization of (6) has been replaced by

$$\begin{aligned} \mathcal{N}_s(\mathbf{u}_h; [\mathbf{u}_h, p_h], [\mathbf{v}_h, q_h])_{\Omega} &= \mathcal{N}(\mathbf{u}_h; [\mathbf{u}_h, p_h], [\mathbf{v}_h, q_h])_{\Omega} \\ &\quad + \mathcal{S}(\mathbf{u}_h; [\mathbf{u}_h, p_h], [\mathbf{v}_h, q_h])_{\Omega}. \end{aligned}$$

The perturbation term  $\mathcal{S}$  introduced by OSS (in its quasi-static form) reads

$$\begin{aligned} \mathcal{S}(\mathbf{u}_h; [\mathbf{u}_h, p_h], [\mathbf{v}_h, q_h])_{\Omega} &= (\tau_1 \Pi^{\perp}(\mathbf{u}_h \cdot \nabla \mathbf{u}_h + \nabla p_h), \mathbf{u}_h \cdot \nabla \mathbf{v}_h + \nabla q_h)_{\Omega} \\ &\quad + (\tau_2 \Pi^{\perp}(\nabla \cdot \mathbf{u}_h), \nabla \cdot \mathbf{v}_h)_{\Omega}. \end{aligned} \quad (13)$$

Here,  $\Pi^{\perp}(\cdot)$  is the  $L^2$  orthogonal projection onto the finite element space, i. e.:  $\Pi^{\perp}(\cdot) = \mathcal{I}(\cdot) - \Pi(\cdot)$ , where  $\Pi(\cdot)$  is the  $L^2$  projection onto the finite element space and  $\mathcal{I}(\cdot)$  the identity operator. For the choice of the stabilization parameters  $\tau_1$  and  $\tau_2$  and for a thorough description of this stabilization technique, we refer to Codina (2002).

Let us denote by  $C_s$  the sum of matrix  $C$  and the corresponding stabilization terms obtained from (13). Similarly, we denote by  $B_s$  ( $B_s^T$ , resp.) the sum of matrix  $B$  ( $B^T$ , resp.) and the corresponding stabilization terms. Moreover, we indicate with  $L_\tau$  the matrix associated with the pressure stabilization. The stabilized fully discrete problem can be written in matrix form (12) with

$$A = \begin{bmatrix} C_s & B_s^T \\ B_s & L_\tau \end{bmatrix}, \quad \mathbf{X}^{n+1} = \begin{bmatrix} \mathbf{U}^{n+1} \\ \mathbf{P}^{n+1} \end{bmatrix}, \quad \mathbf{b}^{n+1} = \begin{bmatrix} \mathbf{b}_u^{n+1} \\ \mathbf{b}_p^{n+1} \end{bmatrix}.$$

For more details concerning the discretization of the Navier-Stokes problem, we refer to, e.g., Quarteroni and Valli (1994).

### 3. Symmetry breaking

In this section, we focus on identifying the critical Reynolds number for the symmetry breaking  $Re_{sb}$  for two different values of the expansion ratio  $\lambda$ . The main aim of this section is to validate our solver against the results reported in Oliveira et al. (2008) and in Drikakis (1997). Once our solver has been validated on a known set of related bifurcation problems, and convergence studies have been performed showing good convergence properties, it can be used as a predictive tool for discovery of new physical phenomena, such as the Hopf bifurcation of the system under consideration.

Let us start with the test case in Oliveira et al. (2008). The geometry under consideration is shown in Fig. 1(a) with the upstream and downstream channel width  $W = 4$ , and contraction width  $w = 0.26$ . Thus, the expansion ratio  $\lambda = W/w$  is 15.4. The length of the contraction  $L_c$  is set to 2. In this domain, we simulate the flow for different Reynolds numbers (ranging from 0.01 to 71.3) to examine the onset of asymmetries in any computational study.

Eq. (1)-(2) are supplemented with the following steady boundary conditions: parabolic velocity profile at the inlet  $\Gamma_{in}$ , stress-free boundary condition at the outlet  $\Gamma_{out}$ , and no-slip condition on the rest of the boundary. The channel upstream of the contraction and the expansion channel need to be long enough so that the flow is fully established when it reaches both the contraction and the outlet section. The fluid is initially at rest. A time marching algorithm is used to approach the steady-state solution. The numerical simulations were stopped when the relative  $L^2$ -norm of the difference of two subsequent solutions was less than a prescribed tolerance  $\epsilon$ :

$$\frac{\|\mathbf{u}_h^{n+1} - \mathbf{u}_h^n\|_{L^2(\Omega)}}{\|\mathbf{u}_h^{n+1}\|_{L^2(\Omega)}} \leq \epsilon \quad \text{and} \quad \frac{\|p_h^{n+1} - p_h^n\|_{L^2(\Omega)}}{\|p_h^{n+1}\|_{L^2(\Omega)}} \leq \epsilon, \quad (14)$$

where  $\mathbf{u}_h^{n+1}$  (resp.,  $\mathbf{u}_h^n$ ) and  $p_h^{n+1}$  (resp.,  $p_h^n$ ) are the computed velocity and pressure at time  $t^{n+1}$  (resp.,  $t^n$ ). The value of  $\epsilon$  was set to  $10^{-8}$ .

In Fig. 2, we report the streamlines at the time when stopping criterion (14) is satisfied for four different values of  $Re$ . For very low Reynolds number (e.g.,  $Re = 0.01$ ), it is impossible to deduce the flow direction from the streamlines: as shown in Fig. 2(a), the flow has both a horizontal and vertical symmetry axis. As the Reynolds number is increased, the Moffatt eddies downstream of the expansion grow while the vortices upstream of the contraction reduce in size: we see in Fig. 2(b) that the flow at  $Re = 7.8$  has lost the symmetry about the vertical axis, while the symmetry about the horizontal axis is maintained. At a further increase of the Reynolds number, the flow exhibits a supercritical bifurcation and it becomes asymmetric also with respect to the horizontal symmetry axis of the domain; see Fig. 2(c) which corresponds to  $Re = 31.1$ . In Fig. 2(c), the lower recirculation enlarged and pushed the high velocity jet to the upper wall. Notice that the flow could have evolved to its reflected image configuration with respect to the domain symmetry axis. A further increase in Reynolds number generates a third vortex downstream on the side of the

smaller primary vortex, as the enlarged one grows and pushes the jet even closer to the wall; see Fig. 2(d). Fig. 2 is in good qualitative agreement with Oliveira et al. (2008).

For a quantitative agreement, we report the bifurcation diagram shown in Fig. 3, which shows the effect of Reynolds number on the length of the recirculation zones formed downstream of the expansion and it is identical to the one presented in Oliveira et al. (2008). The lengths in Fig. 3 ( $r_1$  to  $r_4$ , as marked in Fig. 2(d)) are normalized with respect to the downstream channel width  $W$ . As in Oliveira et al. (2008), the critical Reynolds number for the symmetry breaking  $Re_{sb}$  was found to be approximately 28.5, which is in good agreement also with the results in Mishra and Jayaraman (2002). In fact, reference Mishra and Jayaraman (2002) considers  $\lambda = 16$  and obtains a critical Reynolds number of 27.5, which is very close to what we get. At  $Re$  between 41 and 42, the third vortex appears.

For a further validation of the results, we consider a test case from Drikakis (1997). Since we are only interested in the evolution of the vortices in the expansion channel as  $Re$  varies, we are going to consider the domain reported in Fig. 4(a): the inlet  $\Gamma_{in}$  of this new geometry is the outlet of the contraction channel in Fig. 1(a). Thus  $W = 1$  and contraction width  $w = 1/6$ , which implies  $\lambda = 6$ . This is one of the geometries considered in Drikakis (1997). Note that if the contraction channel length  $L_c$  (see Fig. 1) is enough to have established Poiseuille flow in it, the flow upstream of the contraction is not going to affect the flow downstream. In this domain, we examine the onset of asymmetries by simulating the flow for Reynolds numbers ranging from 0.01 to 73.3.

As boundary conditions, we impose a parabolic velocity profile with maximum velocity  $U_{max} = 1$  on  $\Gamma_{in}$ , a stress-free boundary condition at the outlet  $\Gamma_{out}$ , and no-slip condition on the rest of the boundary. We change the Reynolds number by varying the value of the viscosity  $\mu$ . The stopping tolerance for the fixed point iterations was set to  $10^{-8}$ , since as the Reynolds number increases the convective term needs to be properly resolved.

For this second test case, we checked the influence of the mesh size on the value of  $Re_{sb}$ . Three meshes with different levels of refinement were considered:

- a coarse mesh, with an average element diameter  $h_{avg} = 4 \cdot 10^{-2}$ , a maximum element diameter  $h_{max} = 6 \cdot 10^{-2}$  and a minimum element diameter  $h_{min} = 10^{-2}$ ; this mesh has around  $10^4$  nodes and  $1.9 \cdot 10^4$  triangles;
- a medium mesh, with  $h_{avg} = 2.3 \cdot 10^{-2}$ ,  $h_{max} = 4 \cdot 10^{-2}$ ,  $h_{min} = 7 \cdot 10^{-3}$ ; this mesh has around  $2.2 \cdot 10^4$  nodes and  $4.3 \cdot 10^4$  triangles;
- a fine mesh, with  $h_{avg} = 1.3 \cdot 10^{-2}$ ,  $h_{max} = 2.8 \cdot 10^{-2}$ ,  $h_{min} = 5 \cdot 10^{-3}$ ; this mesh has around  $4.4 \cdot 10^4$  nodes and  $8.7 \cdot 10^4$  triangles.

The minimum diameter was set at the inlet in order to have proper resolution of the contraction. The bifurcation diagram in Fig. 4(b) shows the effect of Reynolds number on the length of the recirculation zones. Since now  $W = 1$ , the normalized lengths correspond to the actual lengths.

From Fig. 4(b) we see that for  $\lambda = 6$  the third recirculation does not appear for  $Re \leq 73.3$ , regardless of the mesh used, while for  $\lambda = 15.4$  it appeared just past  $Re = 41$ . We remark that the results for the medium mesh and the fine mesh are almost superimposed and they both give a value of  $Re_{sb}$  approximately equal to 46.5. Notice that as the aspect ratio  $\lambda$  decreases, the critical Reynolds number for the symmetry breaking increases, as observed also in Drikakis (1997). The bifurcation graph in Fig. 4(b) is very similar to the one in Drikakis (1997), taking into account the fact that we defined the Reynolds number as in (5) with the characteristic velocity  $U = 2U_{max}/3$ , while in Drikakis (1997) the Reynolds number is defined as in (3) with  $L = w$  and  $U = U_{max}$ ,  $U_{max}$  being the maximum inlet velocity. Converting our value  $Re_{sb} = 46.5$  to the system used in Drikakis (1997) we get 34.8, which is very close to 33, the value found in Drikakis (1997). Table 1 shows the values of  $Re_{sb}$  for different levels of mesh refinement. Table 1 and Fig. 4(b) show that if the computations are performed on a mesh that is under-refined, the value of  $Re_{sb}$  gets overestimated.

Keeping  $\lambda = 6$ , we check how the flow structures evolve as  $Re$  is pushed to higher values. In Fig. 5, we report the streamlines at the time when stopping criterion (14) is satisfied for  $Re = 133.3, 266.7, 400$ . As mentioned earlier, the jet can attach to either the upper wall (as for  $Re =$

133.3) or the lower wall (as for  $Re = 266.7, 400$ ).

#### 4. Hopf bifurcation

In contrast with other works, in this work we push our investigation even further, past the symmetry breaking bifurcation. As  $Re$  increases, the long portion of the jet between recirculation 3 and recirculation 4 (see, e.g., Fig. 5(c)) loses its stability and breaks into small vortices that are transported downstreams. To show this phenomenon, we report in Fig. 6 the pressure contour lines for  $Re = 490$  at three different times.

To estimate the value of the critical Reynolds number  $Re_H$  at which the flow becomes time dependent, we have first detected two values of  $Re$ , namely  $Re = 400$  and  $Re = 490$ , for which the asymptotic solution is found to be steady and time-dependent, respectively. This interval, assumed to include the first critical Reynolds number, has been reduced by bisection. We repeated this procedure on the same three meshes as before in order to understand the influence of the mesh size on the value of  $Re_H$  and check convergence in space to a given  $Re_H$ . For all the simulations we used a time step  $\delta t = 10^{-2}$ .

**Remark 1.** *In finding the critical Reynolds number  $Re_H$  the mesh plays a central role, like in every other numerical study. In particular, we noticed that the so called “criss-cross” or British flag mesh has scarce performances. This is confirmed by Picasso et al. (2011), where it is shown that certain methods for approximating second derivatives (i.e., the viscous term) do not exhibit convergence in space on the criss-cross mesh due to its topology. The poor approximation of the viscous term makes the Reynolds number of the simulated flow higher than the imposed value. For this reason, we decided to use unstructured quasi-uniform meshes for our study.*

It has been shown (e.g., in Goodrich et al. (1990); Shen (1990); Autieri et al. (2002)) that in the analysis of unsteady cavity flows the choice of the indicators suitable for monitoring the evolution of the system toward an asymptotic solution represents a critical aspect. In the above references, the total kinetic energy was considered a good indicator of the system dynamics. Thus, we are going to track the total kinetic energy in time:

$$E(t) = \frac{1}{2} \int_{\Omega} |\mathbf{u}_h(t)|^2 d\Omega. \quad (15)$$

It is known (see, e.g., Autieri et al. (2002)) that carrying the simulations to convergence with  $Re$  very close to  $Re_H$  is extremely expensive because the system evolves to its asymptotic state with a velocity that decreases as the Reynolds number approaches its critical value. Therefore, instead of giving the value of  $Re_H$ , for all the meshes under consideration we give a range for  $Re_H$ , which is reported in Table 2. In Table 2, we also report the mean value and amplitude of the kinetic energy oscillation at Reynolds number equal to the upper bound of the range.

With the simulations on the coarse mesh, we narrowed the interval containing  $Re_H$  to  $(413.3, 420)$ : for  $Re = 413.3$  the system evolves towards a steady state, while for  $Re = 420$  the solution is time-dependent. On the medium mesh we found that the interval containing  $Re_H$  is  $(466.7, 473.3)$ , while on the fine mesh we found  $(470.7, 476)$ . We see that the effect of using an insufficiently refined mesh is to underestimate  $Re_H$ . From the coarse mesh to the medium mesh, there is a 11.3% difference in the first Reynolds numbers at which  $E(t)$  shows sustained oscillations for several thousands of time units. From the medium mesh to the fine one, this difference is reduced to 0.5%. As for the mean value of  $E(t)$ , there is a 8.7% difference between values found with the coarse and medium mesh, reduced to 0.07% between the values found with medium and fine mesh (see Table 2). These percentages show a (monotonic) convergence when refining the grid.

Regardless of the mesh, the Hopf bifurcation occurs in the sudden expansion channel at a much smaller Reynolds number than in the lid-driven cavity, where it occurs in the interval

[8017.6, 8018.8) according to Autieri et al. (2002).

In Fig. 7, we report the evolution of the kinetic energy computed on the coarse mesh for  $Re = 413.3$  and  $Re = 420$  over time interval [2000, 3400]. For  $Re = 413.3$ , the amplitude of the oscillations in Fig. 7(a) decreases over time as the system evolves to a steady state, and the stopping criterion (14) is eventually satisfied for  $t \approx 9900$ . For  $Re = 420$  however, the oscillations do not get damped over a long period of time. A zoomed view of the asymptotic oscillatory behavior is shown in Fig. 7(c).

The periodic character of the asymptotic solution can be established by a Fourier analysis of  $E(t)$ . Fig. 8(a) displays the power spectral density of  $E(t)$  for  $Re = 420$ , obtained from a time series of 60,000 points over a time interval of size 600. We see that in Fig. 8(a) there is one isolated peak corresponding to frequency  $f_c = 0.075$ , showing that the asymptotic oscillations have only one fundamental frequency.

The periodic solution can be represented also in the two-dimensional phase plane. Fig. 8(b) shows the phase portrait having  $E(t)$  on the horizontal axis and  $E(t + \tau)$  on the vertical one, with  $\tau = 0.73$ .

Next, we are going to consider the results obtained on the medium mesh. In Fig. 9, we report the asymptotic evolution of the kinetic energy for  $Re = 466.7$  and  $Re = 473.3$ . For  $Re = 466.7$ ,  $E(t)$  initially displays oscillations (see Fig. 9(a)), but as time passes the oscillations are damped out as shown in Fig. 9(b). Among the Reynolds number we considered, the first one at which the oscillations do not get damped over time is  $Re = 473.3$ . However, as shown in Fig. 9(c), the oscillations are not simply periodic with one frequency, as the ones reported in Fig. 7(c).

This is confirmed by the power spectral density of  $E(t)$  for  $Re = 473.3$  in Fig. 10(a): the graph shows three main peaks for frequencies 0.02, 0.0375, and 0.075, the first two of which are independent while the third is a multiple of the second one. Thus, the asymptotic oscillations are quasi-periodic. With the medium mesh we were not able to observe sustained monochromatic oscillations for several thousands time units at a given value of Reynolds number. A possible explanation is that the second Hopf bifurcation is very close to the first Hopf bifurcation, so it is not easy to isolate a Reynolds number between the two.

The two-dimensional phase portrait of the asymptotic oscillations of  $E(t)$  for  $Re = 473.3$  is shown in Fig. 10(b). Again, we set the value of  $\tau = 0.73$ . Being the signal quasi-periodic, it is not surprising that the 2D phase portrait in Fig. 10(b) is more complex than one in Fig. 8(b), which is associated to a periodic signal.

Finally, in Fig. 11 we show the evolution of the kinetic energy computed on the fine mesh for  $Re = 470.7$  and  $Re = 476$ . For  $Re = 470.7$ , the  $E(t)$  initially displays oscillations, as shown in Fig. 11(a). Around  $t = 1900$ , the oscillations start to be damped out rapidly and the system evolves towards a steady state, as shown in Fig. 11(b). Among the Reynolds numbers that we considered, the first one at which the oscillations continue till  $t = 4000$  is  $Re = 476$ . As it happened for the medium mesh, these oscillations are quasi periodic. In fact, from the power spectral density in Fig. 12(a), we see that the three main peaks are associated to frequencies 0.02, 0.0375, and 0.075. These are the same frequencies having power peaks in Fig. 10(a). Similarly, the two-dimensional phase portrait of the asymptotic oscillations of  $E(t)$  for  $Re = 476$  reported in Fig. 12(b) resembles the one in Fig. 10(b).

**Remark 2.** *As mentioned in Sec. 3, the homogeneous Neumann condition imposed at the outlet requires the domain to be long enough so that the flow is fully established when it reaches the outlet section. For the results in this section, we took a domain length equal to 30 times the domain height  $W$ . The horizontal and vertical components of the velocity along the domain axis for  $Re = 490$  are plotted in Fig. 13, showing that the flow is fully established for domain length  $30W$ . Indeed, both the horizontal and vertical components reach a plateau.*

*It was also observed in Fortin et al. (1997) that a domain length of  $30W$  is appropriate for  $Re$  less than a thousand. A shorter domain would not only be inconsistent with the outlet condition, but it would modify the shape of the recirculations which are not free to evolve. As a result, one would find*

different values for  $Re_{sb}$  and  $Re_H$ . For instance, when we performed the hydrodynamics stability study using a domain length  $10W$  and a mesh size  $h = 6 \cdot 10^{-2}$ , we found  $Re_H$  of approximately 263, which is slightly more than half of  $Re_H$  found for domain length  $30W$  with a comparable mesh.

We have seen that the coarse mesh we adopted led to an underestimation of the critical Reynolds number and the mean value of the associated  $E(t)$  by 10%, roughly. Other physical quantities are more grossly underestimated by a coarse mesh. An example is enstrophy, which is defined as:

$$\mathcal{E}(t) = \frac{1}{2} \int_{\Omega} |\omega_h(t)|^2 d\Omega, \quad (16)$$

where  $\omega_h$  is the computed vorticity. The enstrophy represents the intensity of rotation of a flow and it is a relevant quantity in turbulent flows. Fig. 14 shows the evolution of the enstrophy computed on the coarse mesh for  $Re = 420$ , on the medium mesh for  $Re = 473.3$ , and on the fine mesh for  $Re = 476$ . The evolutions of  $\mathcal{E}(t)$  computed on the medium and fine mesh are almost superimposed over the whole time interval under consideration. On the other hand, the mean value of  $\mathcal{E}(t)$  computed on the coarse mesh is 27.2% smaller.

Finally, we analyzed the spectrum of the enstrophy oscillations. Fig. 15 displays the power spectral density for the same meshes and Reynolds numbers in Fig. 14. The enstrophy spectrum shows peaks for the same frequency of the kinetic energy spectrum.

## 5. Conclusions

We presented a numerical study for bifurcation phenomena in symmetric plane contraction-expansion channels. The dynamics of this system was analyzed by means of direct numerical simulation of the unsteady two-dimensional NavierStokes equations. Laminar flow calculations were performed for two values of the expansion ratio,  $\lambda = 15.4$  and  $\lambda = 6$ , and several Reynolds numbers.

In contraction-expansion channels, a steady symmetric flow is observed for sufficiently small value of the Reynolds number. Above a certain critical Reynolds number, a steady asymmetric solution is observed: recirculation zones of different sizes form on the upper and lower wall. We validated the critical Reynolds number for the symmetry-breaking bifurcation given by our computations against the value in Oliveira et al. (2008) for  $\lambda = 15.4$  and the value in Drikakis (1997) for  $\lambda = 6$ . Excellent agreement was found.

For  $\lambda = 6$ , we studied the evolution of the flow as the Reynolds number is increased past the symmetry-breaking bifurcation. The computations revealed that, as the Reynolds numbers increases, the system initially continues to evolve towards a steady state and the flow exhibits more and more complex flow structures. At a further increase of the Reynolds number, the flow becomes unsteady, which indicates a Hopf bifurcation. By means of a bisection technique we were able to locate the critical Reynolds number for the Hopf bifurcation in the range (470.7, 476). We analyzed the time evolution of the kinetic energy of the system at different Reynolds numbers in order to extract the power spectral density and the 2D portrait of the system in the phase space.

Finally, we investigated the effect of mesh refinement on the critical Reynolds number for both symmetry-breaking and Hopf bifurcations. Three meshes with different level of refinement were considered. Computations on a under-refined mesh led to an overestimation of the critical Reynolds number for the symmetry-breaking and an underestimation of the critical Reynolds number for the Hopf bifurcation.

## Acknowledgements

This research has been supported in part by the National Science Foundation under grants DMS-1318763, DMS-1311709, and DMS-0806941 (Canic), DMS-1262385 and DMS-1109189 (Canic and Quaini), and by the Texas Higher Education Board (ARP-Mathematics) 003652-0023-2009 (Canic and Glowinski).

## References

- Autieri, F., N. Parolini, and L. Quartapelle (2002). Numerical investigation on the stability of singular driven cavity flow. *Journal of Computational Physics* 183, 1–25.
- Battaglia, F., S. Tavener, A. Kulkarni, and C. Merkle (1997). Bifurcation of low Reynolds number flows in symmetric channels. *AIAA J.* 35, 99–105.
- Bayly, B., S. Orszag, and T. Herbert (1988). Instability mechanisms in shear-flow transition. *Ann. Rev. Fluid Mech.* 20, 359–391.
- Cherdron, W., F. Durst, and J. Whitelaw (1978). Asymmetric flows and instabilities in symmetric ducts with sudden expansions. *J. Fluid Mech.* 84, 13–31.
- Codina, R. (2002). Stabilized finite element approximation of transient incompressible flows using orthogonal subscales. *Comput. Methods Appl. Mech. Engrg.* 191, 4295–4321.
- Davis, T. and I. Duff (1997). An unsymmetric-pattern multifrontal method for sparse LU factorization. *SIAM. J. Matrix Anal. & Appl.* 18(1), 140–158.
- Dijkstra, H., F. Wubs, A. Cliffe, E. Doedel, I. F. Dragomirescu, B. Eckhardt, A. Gelfgat, A. Hazel, V. Lucarini, A. Salinger, E. Phipps, J. Sanchez-Umbria, H. Schuttelaars, L. Tuckerman, and U. Thiele (2014). Numerical bifurcation methods and their application to fluid dynamics: analysis beyond simulation. *Commun. Comput. Phys.* 15, 1–45.
- Drikakis, D. (1997). Bifurcation phenomena in incompressible sudden expansion flows. *Phys. Fluids* 9(1), 76–87.
- Durst, F., A. Melling, and J. Whitelaw (1974). Low Reynolds number flow over a plane symmetric sudden expansion. *J. Fluid Mech.* 64, 111–128.
- Fearn, R., T. Mullin, and K. Cliffe (1990). Nonlinear flow phenomena in a symmetric sudden expansion. *J. Fluid Mech.* 211, 595–608.
- Fortin, A., M. Jardak, J. Gervais, and R. Pierre (1997). Localization of hopf bifurcations in fluid flow problems. *Int. J. Numer. Meth. Fluids* 24, 1185–1210.
- Ginghina, C. (2007). The Coanda effect in cardiology. *J. Cardiovasc. Med.* 8, 411–413.
- Goodrich, J., K. Gustafson, and K. Halasi (1990). Hopf bifurcation in the driven cavity. *Journal of Computational Physics* 90, 219–261.
- Hawa, T. and Z. Rusak (2001). The dynamics of a laminar flow in a symmetric channel with a sudden expansion. *J. Fluid Mech.* 436, 283–320.
- Lanzerstorfer, D. and H. Kuhlmann (2012). Global stability of multiple solutions in plane sudden-expansion flow. *Journal of Fluid Mechanics* 702, 378–402.
- Mishra, S. and K. Jayaraman (2002). Asymmetric flows in planar symmetric channels with large expansion ratios. *Int. J. Num. Meth. Fluids* 38, 945–962.
- Moffatt, H. (1964). Viscous and resistive eddies near a sharp corner. *J. Fluid Mech.* 18, 1–18.
- Oliveira, M., L. Rodd, G. McKinley, and M. Alves (2008). Simulations of extensional flow in microrheometric devices. *Microfluid Nanofluid* 5, 809–826.
- Picasso, M., F. Alauzet, H. Borouchaki, and P. George (2011). A numerical study of some Hessian recovery techniques on isotropic and anisotropic meshes. *SIAM. J. Sci. Comput.* 33(3), 1058–1076.
- Quaini, A., S. Canic, G. Guidoboni, R. Glowinski, S. Igo, C. Hartley, W. Zoghbi, and S. Little (2010). Numerical simulation of an ultrasound imaging model of mitral valve regurgitation. *Cardiology* (115), 251–293.
- Quarteroni, A., R. Sacco, and F. Saleri (2007). *Numerical Mathematics*. Springer Verlag.
- Quarteroni, A. and A. Valli (1994). *Numerical Approximation of Partial Differential Equations*. Springer-Verlag.
- Revuelta, A. (2005). On the two-dimensional flow in a sudden expansion with large expansion ratios. *Phys.*

- Fluids* 17(1), 1–4.
- Serrin, J. (1959). *Mathematical principles of classical fluid mechanics*, Volume Handbuch der Physik, vol. VIII/1, pp. 125–263. Springer Verlag, Berlin.
- Shapira, M., D. Degani, and D. Weihs (1990). Stability and existence of multiple solutions for viscous flow in suddenly enlarged channels. *Comp. Fluids* 18, 239–258.
- Shen, J. (1990). Hopf bifurcation of the unsteady regularized driven cavity flow. *Journal of Computational Physics* 90, 228–245.
- Sobey, I. and P. Drazin (1986). Bifurcations of two-dimensional channel flows. *J. Fluid Mech.* 171, 263–287.
- Wang, Y., A. Quaini, S. Canic, and S. Little (2015). Coanda effect in mitral valve regurgitation: A numerical study. *In preparation..*
- Wille, R. and H. Fernholz (1965). Report on the first European mechanics colloquium on Coanda effect. *J. Fluid Mech.* 23, 801–819.

	coarse mesh	medium mesh	fine mesh	result in Drikakis (1997)
$Re_{sb}$	36	34.8	34.8	33

Table 1. Critical Reynolds number  $Re_{sb}$  for symmetry breaking. Our reported values were converted to the system used in Drikakis (1997).

mesh	range of $Re_H$	mean value of $E(t)$	amplitude
coarse	$413.3 < Re_H < 420$	0.3701	$2.5 \cdot 10^{-4}$
medium	$466.7 < Re_H < 473.3$	0.4054	$2.3 \cdot 10^{-3}$
fine	$470.7 < Re_H < 476$	0.4057	$2.4 \cdot 10^{-3}$

Table 2. Range of critical Reynolds number  $Re_H$ , mean value and amplitude of kinetic energy oscillation at a Reynolds number equal to the upper bound of the range for the meshes under consideration.

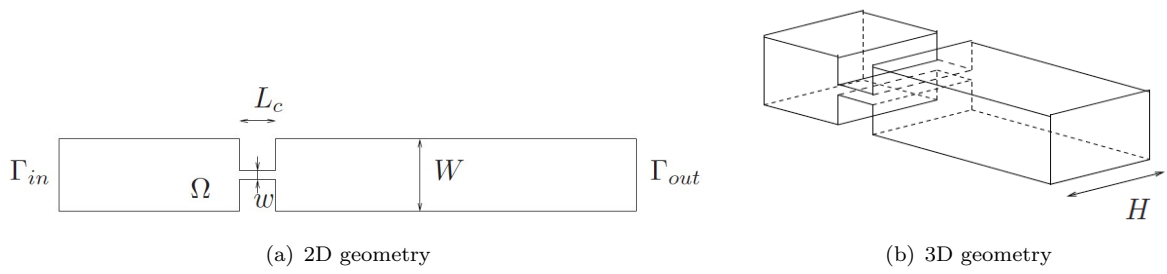


Figure 1. (a) The computational domain considered in Oliveira et al. (2008), which is the limit case of the 3D geometry in (b) for  $H \rightarrow \infty$ .

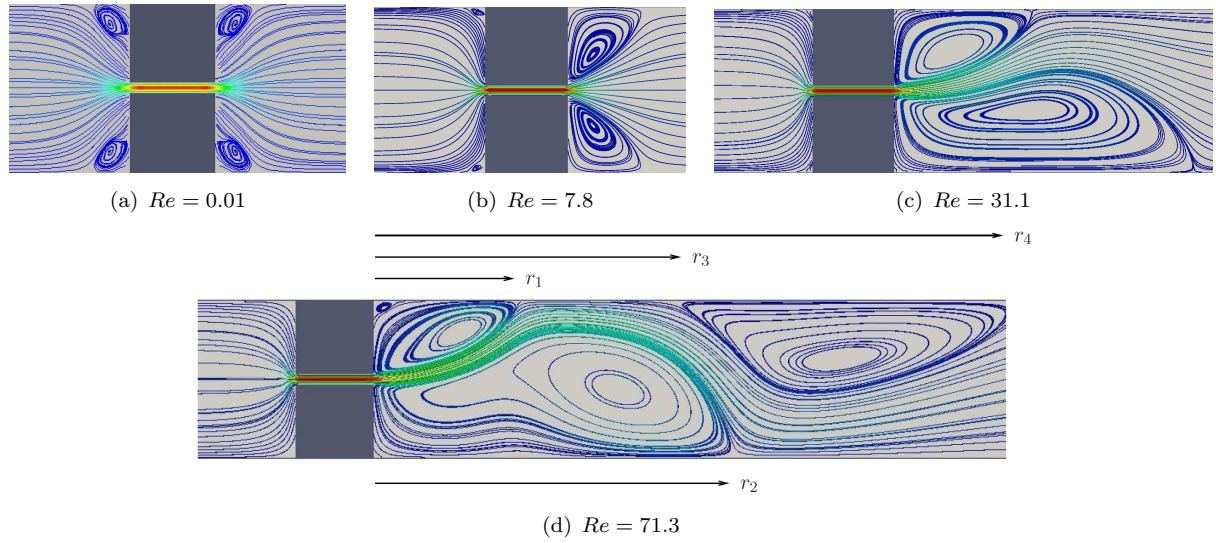


Figure 2. Expansion ratio  $\lambda = 15.4$ : Streamlines at the time when stopping criterion (14) is satisfied for Reynolds numbers (a)  $Re = 0.01$ , (b)  $Re = 7.8$ , (c)  $Re = 31.1$ , (d)  $Re = 71.3$ . The streamlines are colored with the velocity magnitude, with blue corresponding to 0 and red corresponding to 1.

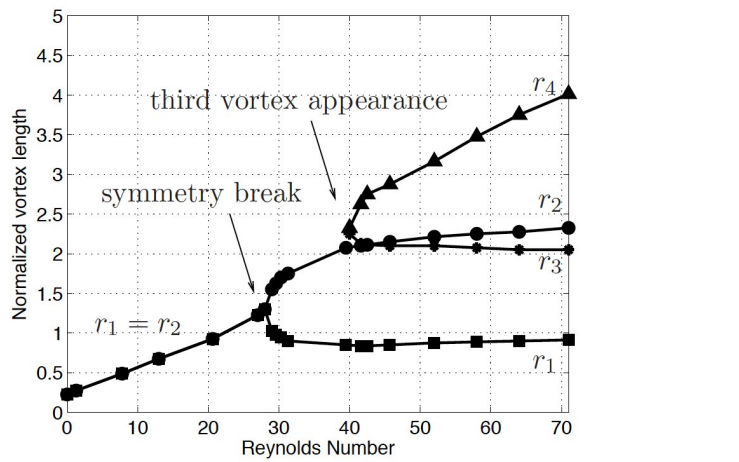


Figure 3. Expansion ratio  $\lambda = 15.4$ : bifurcation diagram for the geometry shown in Fig. 1(a).

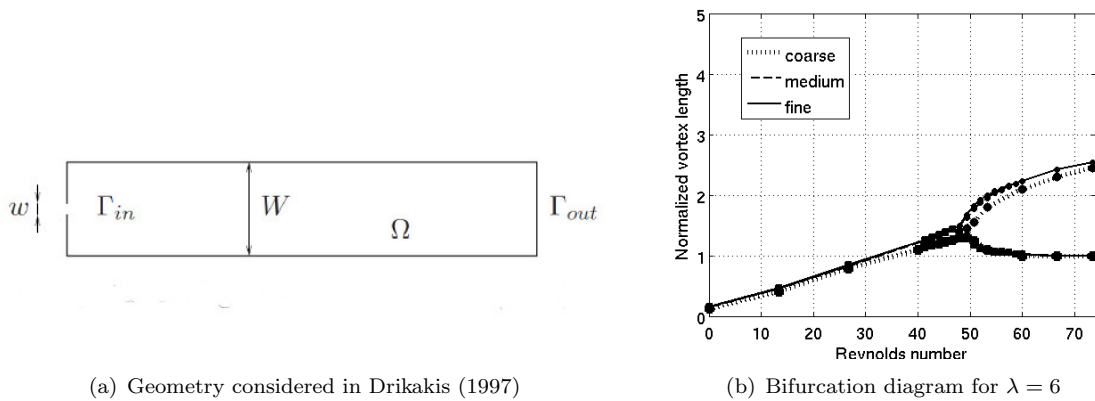


Figure 4. (a) Computational geometry considered in Drikakis (1997) and (b) a convergence study for the bifurcation diagram corresponding to the 2D flow in such geometry with  $\lambda = 6$ . The results refer to three different meshes: coarse, medium, and fine.

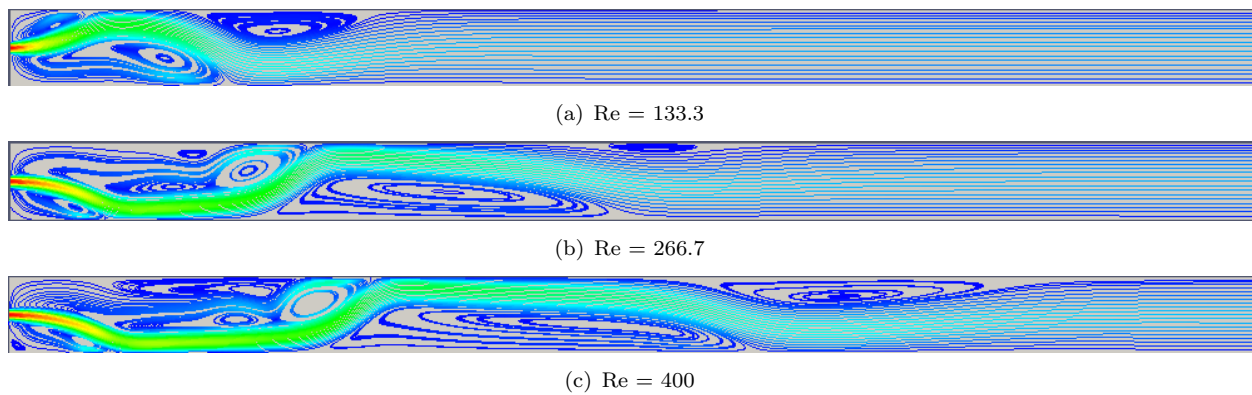


Figure 5. Expansion ratio  $\lambda = 6$ : Streamlines at the time when stopping criterion (14) is satisfied for Reynolds numbers (a)  $Re = 133.3$ , (b)  $Re = 266.7$ , (c)  $Re = 400$ . The streamlines are colored with the velocity magnitude, with blue corresponding to 0 and red corresponding to 1.

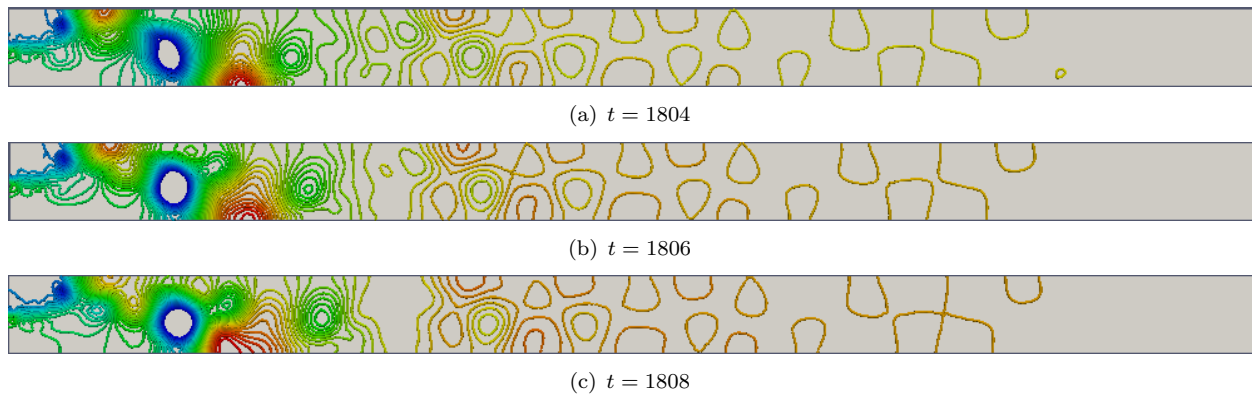


Figure 6. Expansion ratio  $\lambda = 6$ : pressure contour lines for  $Re = 490$  at times (a)  $t = 1804$ , (b)  $t = 1806$ , (c)  $t = 1808$ . The contour lines are colored with the pressure, ranging from -0.095 (blue) to 0.035 (red).

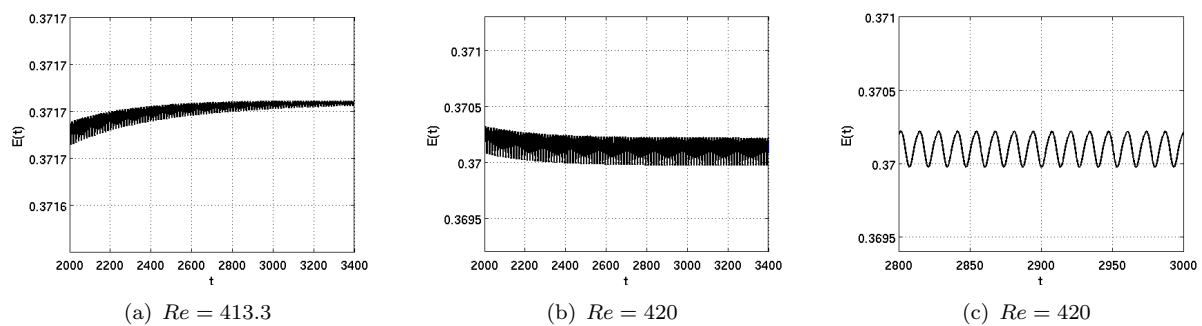


Figure 7. Expansion ratio  $\lambda = 6$ , coarse mesh: evolution of the kinetic energy  $E(t)$ ,  $t \in [2000, 3400]$ , for (a)  $Re = 413.3$  and (b)  $Re = 420$ . (c)  $Re = 420$ : zoom in for  $t \in [2800, 3000]$ .

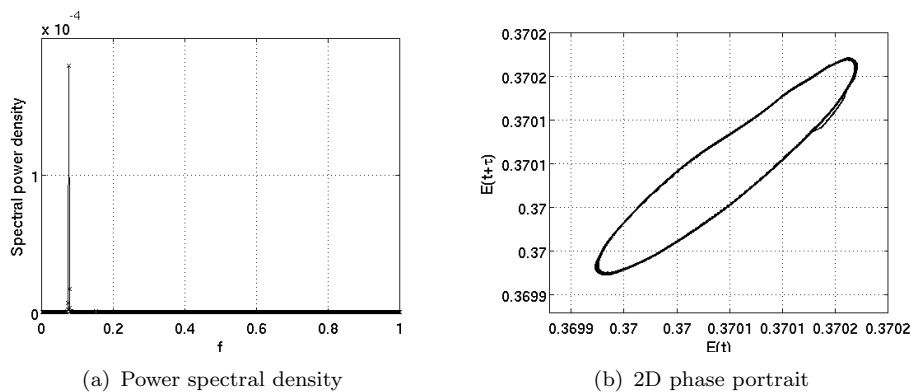


Figure 8. Expansion ratio  $\lambda = 6$ , coarse mesh,  $Re = 420$ : (a) power spectral density and (b) two-dimensional phase portrait of  $E(t)$ .

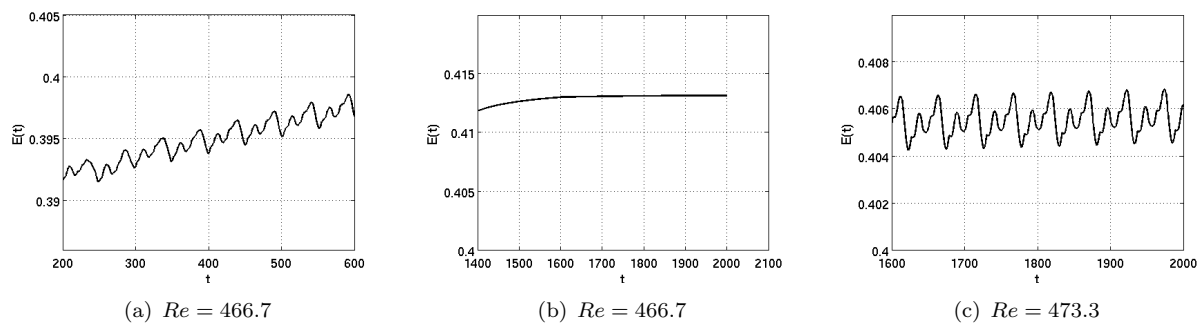


Figure 9. Expansion ratio  $\lambda = 6$ , medium mesh: asymptotic evolution of the kinetic energy  $E(t)$  for (a)  $Re = 466.7$ : zoom in for  $t \in [200, 600]$ , (b)  $Re = 466.7$  for  $t \in [1400, 2000]$ , and (c)  $Re = 473.3$ .

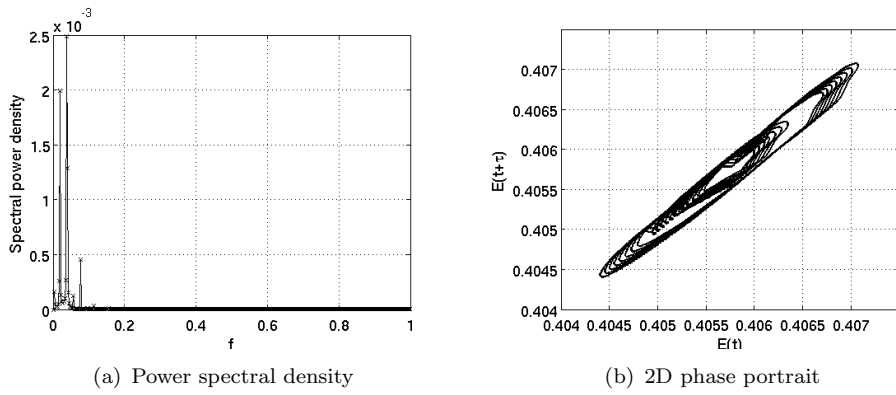


Figure 10. Expansion ratio  $\lambda = 6$ , medium mesh,  $Re = 473.3$ : (a) power spectral density and (b) two-dimensional phase portrait of  $E(t)$ .

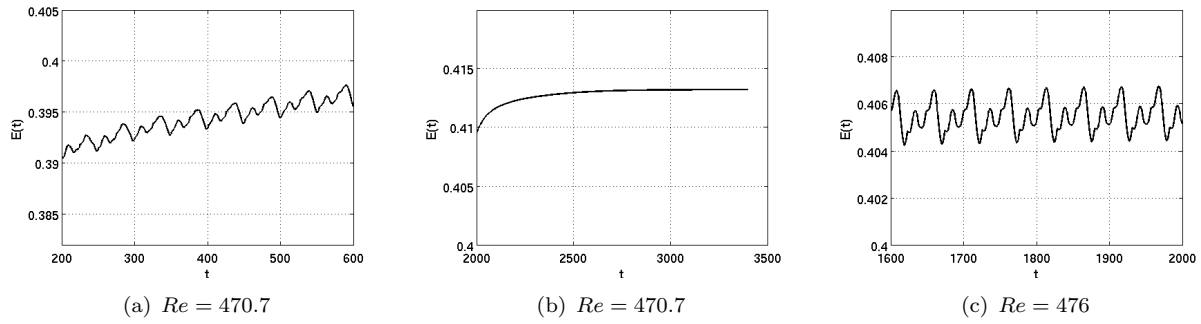


Figure 11. Expansion ratio  $\lambda = 6$ , fine mesh: asymptotic evolution of the kinetic energy  $E(t)$  for (a)  $Re = 470.7$ : zoom in for  $t \in [200, 600]$  (b)  $Re = 470.7$  for  $t \in [2000, 3500]$ , and (c)  $Re = 476$ .

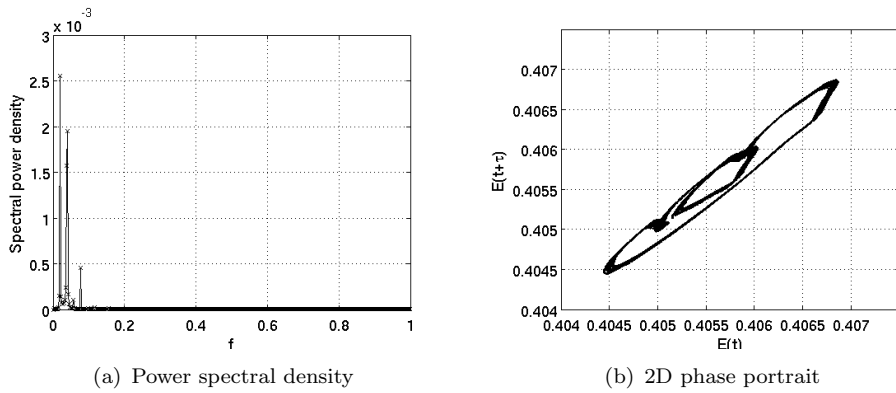


Figure 12. Expansion ratio  $\lambda = 6$ , fine mesh,  $Re = 476$ : (a) power spectral density and (b) two-dimensional phase portrait of  $E(t)$ .

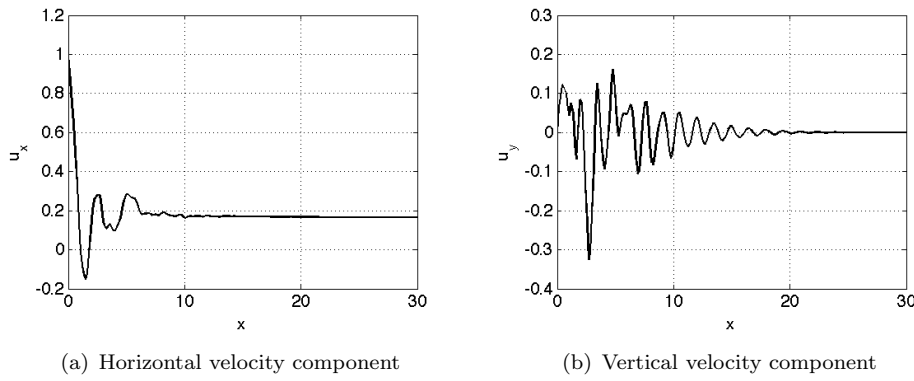


Figure 13. Expansion ratio  $\lambda = 6$ : (a) Horizontal and (b) vertical velocity components along the domain horizontal axis for  $Re = 490$ .

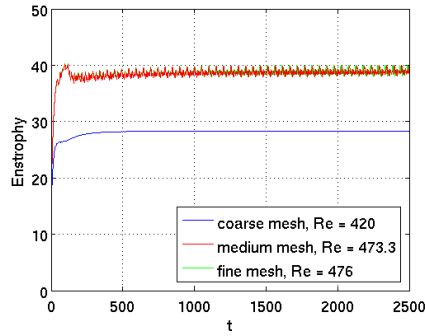


Figure 14. Expansion ratio  $\lambda = 6$ : evolution of the enstrophy computed on the coarse mesh for  $Re = 420$ , on the medium mesh for  $Re = 473.3$ , and on the fine mesh for  $Re = 476$ .

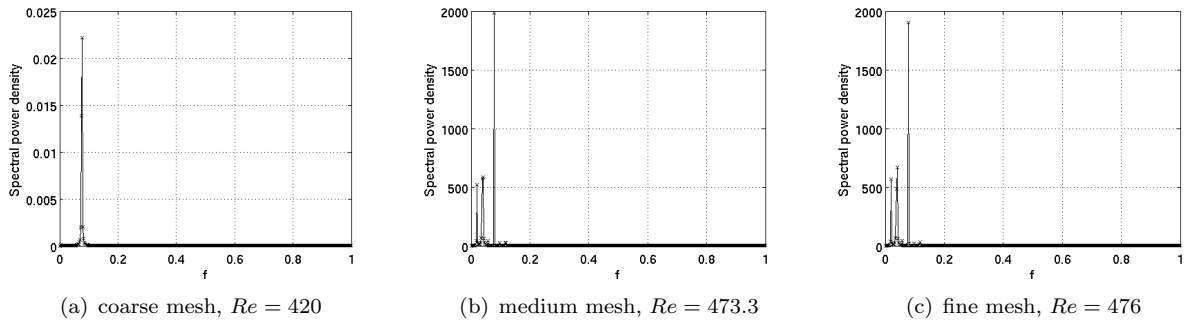


Figure 15. Expansion ratio  $\lambda = 6$ : power spectral density for the enstrophy (a) for  $Re = 420$  on the coarse mesh, (b)  $Re = 473.3$  on the medium mesh and (c)  $Re = 476$  on the fine mesh.